



In materia reservoir computing with a fully memristive architecture based on self-organizing nanowire networks

Gianluca Milano¹✉, Giacomo Pedretti², Kevin Montano³, Saverio Ricci², Shahin Hashemkhani¹✉, Luca Boarino¹, Daniele Ielmini²✉ and Carlo Ricciardi³✉

Neuromorphic computing aims at the realization of intelligent systems able to process information similarly to our brain. Brain-inspired computing paradigms have been implemented in crossbar arrays of memristive devices; however, this approach does not emulate the topology and the emergent behaviour of biological neuronal circuits, where the principle of self-organization regulates both structure and function. Here, we report on *in materia* reservoir computing in a fully memristive architecture based on self-organized nanowire networks. Thanks to the functional synaptic connectivity with nonlinear dynamics and fading memory properties, the designless nanowire complex network acts as a network-wide physical reservoir able to map spatio-temporal inputs into a feature space that can be analysed by a memristive resistive switching memory read-out layer. Computing capabilities, including recognition of spatio-temporal patterns and time-series prediction, show that the emergent memristive behaviour of nanowire networks allows *in materia* implementation of brain-inspired computing paradigms characterized by a reduced training cost.

In parallel with progress in neuroscience, growing interest has been devoted to electronic neuromorphic systems aimed at emulating the human brain functionality and effectiveness¹. To fulfil this goal, memristive devices capable of adaptation in response to electrical stimuli have been recently adopted as artificial synapses for hardware implementation of non-von-Neumann computing^{2–5}. In this framework, memristive circuits realized with a top-down approach and organized into rigid grid-like crossbar arrays have been proposed for the hardware demonstration of artificial neural networks^{6,7}. A key issue of top-down topologies that emphasize the role of individual elements is the lack of similarity with respect to biological neural systems, where the principle of self-organization governs both structure and function and the high synaptic connectivity in between neurons provides adaptability, fault tolerance and robustness⁸. Indeed, learning, memory and intelligence arise from the complexity of neuronal systems and the interplay between the human brain structure and function^{9,10}. Inspired by the recurrent connectivity of biological neural networks, nanoarchitectures based on many interacting nano-parts have been proposed as alternatives for biologically plausible computing hardware^{11–24}. By emphasizing the network architecture as a whole, these self-organized systems appear as the most promising platform for *in materia* implementation of brain-inspired reservoir computing (RC) by exploiting the emergent dynamics of the whole system with no need for fine tuning of its constituent elements. In this unconventional computing framework derived from recurrent neural network models such as echo state networks²⁵ and liquid state machines²⁶, the reservoir usually consists of a massive network of coupled nonlinear elements that map the input signals into a feature space that is then analysed by a read-out function. Since training is limited at the read-out, the RC system benefits from low-cost training, high versatility and

fast learning^{27,28}. RC has been recently implemented in hardware by exploiting the complex dynamics of spintronic oscillators²⁹, magnetic skyrmions³⁰, photonic systems^{31,32} and top-down memristive cells^{33–37}. Although physical reservoirs based on self-organized nano-networks have been experimentally realized^{16,20,24}, *in materia* implementation of RC in fully memristive systems based on self-organized nano-objects emulating the neuromorphic type of data processing of the human brain still represents a challenge.

Here, we experimentally demonstrate *in materia* RC in a fully memristive architecture based on self-organized nanowire (NW) networks exploited as network-type physical reservoirs with random connections among multiple nonlinear memristive elements, to mimic the core principle of RC. The NW network with nonlinear dynamics and fading memory properties allows spatio-temporal processing of multi-terminal inputs thanks to the functional synaptic connectivity of the system with mutual electrochemical interactions among memristive NW junctions. The emergent dynamics of the physical reservoir state, represented by the conductivity map of the NW network, can project a spatio-temporal input pattern in a feature space that can be analysed by a memristive read-out based on resistive switching memory (ReRAM) devices. We show that such versatile, bio-inspired and low-cost training architecture is able to perform recognition of spatio-temporal patterns and to predict chaotic time series. Similar to the human brain, the proposed fully memristive architecture is capable of processing the temporal and spatial nature of the input signal, paving the way to intelligent systems based on the combination of different neuromorphic hardware technologies.

A conceptual schematization of the RC paradigm is reported in Fig. 1a. Here, the role of the reservoir is to nonlinearly map a time-dependent input $u(t)$ into a feature space represented by the

¹Advanced Materials Metrology and Life Sciences Division, Istituto Nazionale di Ricerca Metrologica, Turin, Italy. ²Dipartimento di Elettronica, Informazione e Bioingegneria, Politecnico di Milano and IU.NET, Milan, Italy. ³Department of Applied Science and Technology, Politecnico di Torino, Turin, Italy.

✉e-mail: g.milano@inrim.it; daniele.ielmini@polimi.it; carlo.ricciardi@polito.it

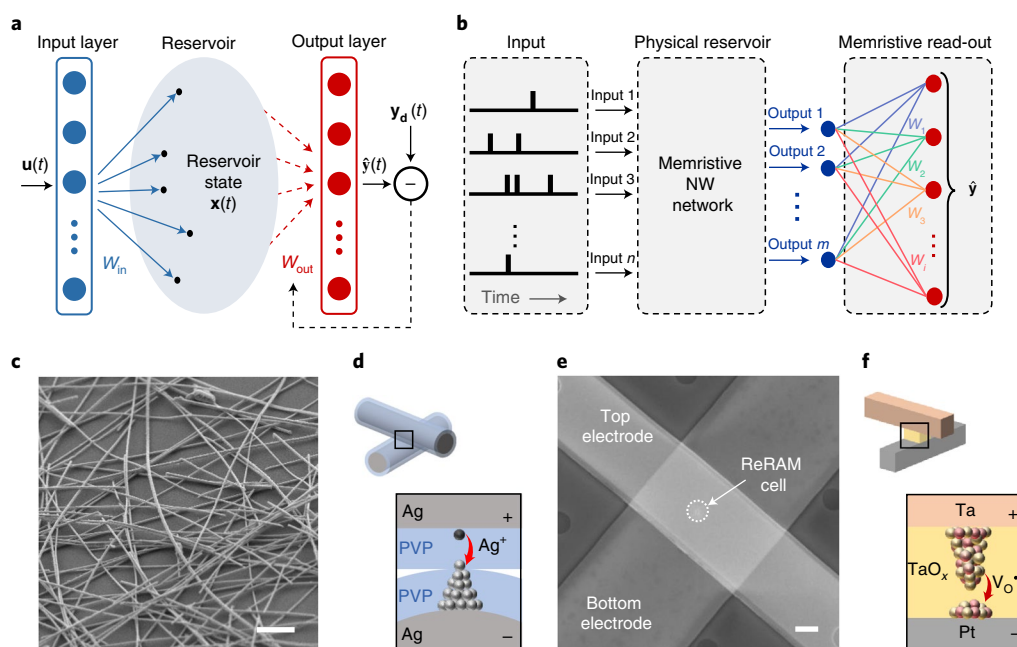


Fig. 1 | Physical RC based on memristive NW networks. **a**, Schematic representation of the RC paradigm where the reservoir maps the input $u(t)$ through input weights W_{in} into a higher dimensional space that is then analysed by a read-out function. The read-out weights (W_{out}) are the only ones to be trained by comparing the output $\hat{y}(t)$ with the desired output $y_d(t)$. **b**, Schematic representation of RC implementation in a fully memristive nanoarchitecture where an input encoded in n pulse streams is processed by the NW network physical reservoir. Then, the physical reservoir state represented by m outputs is analysed by the memristive read-out neural network, where synaptic weights W_i are implemented in hardware with ReRAM devices. **c**, Scanning electron microscopy (SEM) image of a highly interconnected memristive NW network reservoir (scale bar, 2 μm). **d**, Schematic representation of the resistive switching mechanism occurring at the NW junctions, where the conductivity can be modulated by the formation/rupture of a metallic Ag conductive path across the NW shell layer, under the action of the applied electric field. **e**, SEM image of a TaO_x ReRAM cell at the cross-point between top and bottom electrodes (scale bar, 2 μm). **f**, Schematic representation of the working principle of the TaO_x ReRAM cell based on the formation/rupture of a substoichiometric conductive filament rich in oxygen vacancies ($\text{V}_\text{O}^{\bullet\bullet}$). Yellow spheres represent the metal oxide in a reduced valence state, while red spheres represent oxygen vacancies.

reservoir internal state $x(t)$, such that the input features can be recognized by a simple classification algorithm in the read-out, where output weights are the only ones to be trained by comparing the output $\hat{y}(t)$ with the desired output $y_d(t)$ (refs. 27,28). The RC hardware implementation is schematized in Fig. 1b, where the memristive NW network dynamics are exploited for the realization of a physical reservoir able to process time-dependent inputs, and reservoir outputs are then analysed by a memristive neural network read-out. The physical reservoir consisting of a highly interconnected and designless memristive NW network (Fig. 1c) was realized with a low-cost bottom-up approach by drop-casting Ag NWs in suspension on an insulating substrate (Supplementary Fig. 1 and Methods). The emergent NW network dynamics upon electrical stimulation arise from the mutual interaction of a multitude of memristive NW cross-point junctions. Indeed, an electrochemical potential difference across intersecting NWs induces anodic dissolution of Ag to form Ag^+ ions that migrate in the polyvinylpyrrolidone (PVP) insulating NW shell layer to form a conductive bridge that regulates the junction conductivity (Fig. 1d)¹². The memristive neural network read-out is implemented in hardware by mapping synaptic weights associated with each output neuron in the analogue conductance levels of an array of TaO_x ReRAM cross-point devices (Fig. 1e and Supplementary Fig. 2), where resistive switching relies on the formation/rupture of a substoichiometric conductive filament (Fig. 1f, Supplementary Note 1 and Supplementary Fig. 3).

The formation upon electrical stimulation and the subsequent spontaneous dissolution of the conductive bridges at NW junctions are responsible for emergent nonlinear dynamics and fading

memory properties (short-term memory) of the physical reservoir. Indeed, as can be observed in Fig. 2a, stimulation of the network in between two terminals upon constant voltage bias leads to the progressive potentiation (facilitation) of the effective network conductance (Fig. 2a). After stimulation, the network spontaneously relaxes back to the ground state, as a consequence of the volatile behaviour of memristive junctions (Supplementary Note 2)¹². These nonlinear network dynamics with fading memory properties can be modelled by mapping the NW network into a weighted grid graph (Supplementary Fig. 4 and Supplementary Note 3), where the transient behaviour of each memristive edge is regulated by short-term memory effects described by a potentiation–depression rate balance equation (Supplementary Note 4). The model proposed here allows us (1) to interpolate the evolution over time of the network effective conductance (Fig. 2a), and (2) to visualize the resulting spatio-temporal evolution of the conductive pathway when electrically stimulated in different spatial locations (Fig. 2b and Supplementary Video 1). As can be observed, simulations evidence the growth of a conductive pathway connecting the two stimulated areas of the network, followed by the gradual relaxation to the conductance ground state (Fig. 2b), in accordance with experimental observations of the formation of a localized conductive pathway connecting stimulated NW network areas^{38,39}. Importantly, experimental data show that the change of the effective conductance (Δw) after pulse stimulation and the following relaxation behaviour can be controlled by properly adjusting the pulse width and amplitude. Figure 2c reports the change in the effective conductance at the end of a single pulse stimulation with pulses of different lengths and

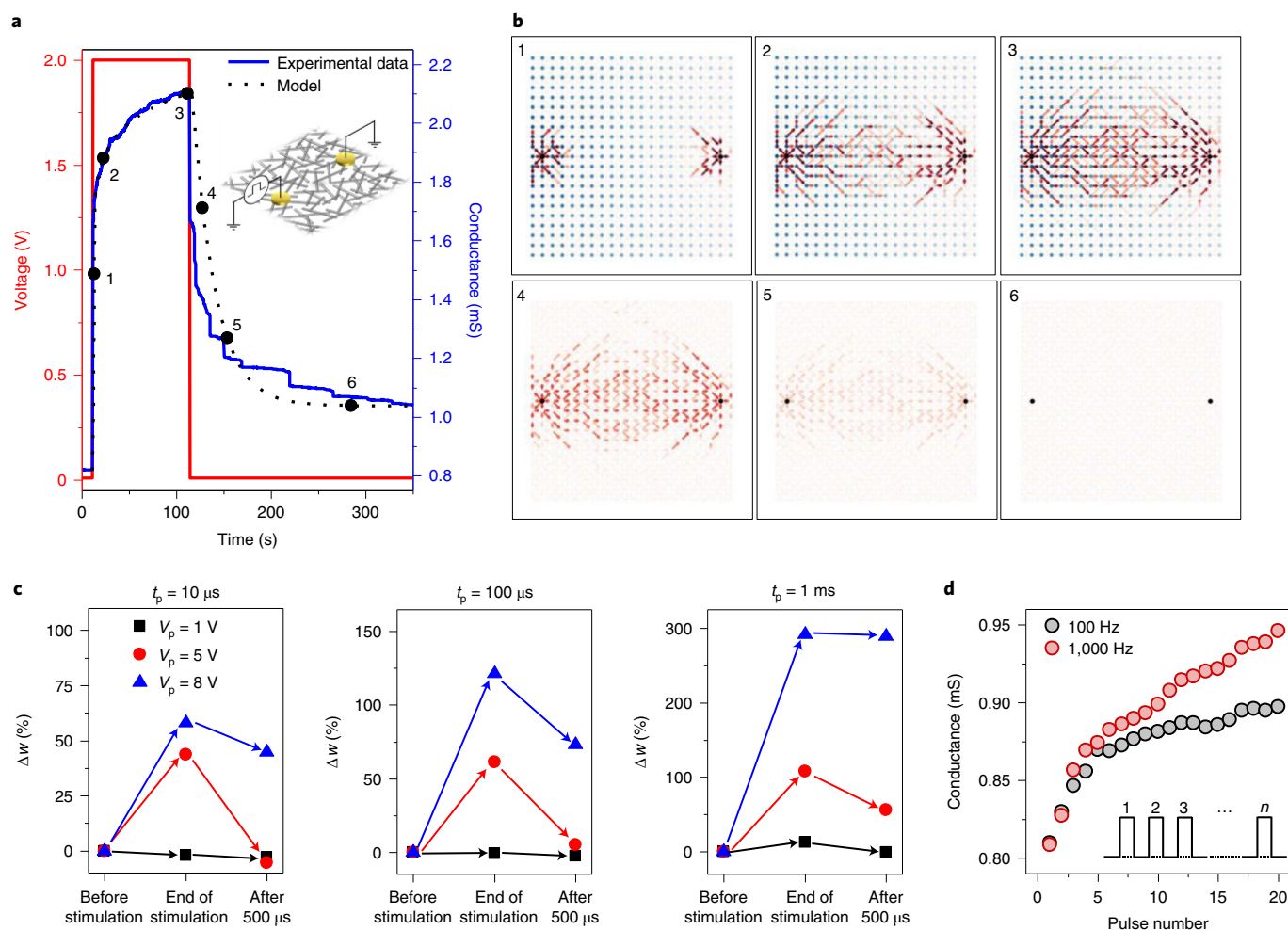


Fig. 2 | Nonlinear dynamics and fading memory properties of the memristive NW network reservoir. **a**, Experimental and simulated potentiation and subsequent spontaneous relaxation of the effective conductance upon voltage pulse stimulation (2 V, 100 s) in a two-terminal configuration, as schematized in the inset. **b**, Spatio-temporal evolution of the conductive path formation and following dissolution according to the grid-graph network model where the short-term conductance dynamics of each edge are modelled through a potentiation-depression rate balance equation. Red intensity of edges is proportional to the edge conductance and blue intensity of each node is proportional to the node voltage, while arrows indicate the current direction and black nodes represent input pads. The left electrode was biased, while the right one was kept as ground. The numbers correspond to the numbers in **a**. **c**, Change in the conductance weight of the network in the two-terminal configuration at the end of a single pulse stimulus and after 500 μ s, for a stimulation pulse length (t_p) of 10 μ s, 100 μ s and 1 ms with different pulse amplitudes (V_p). **d**, Gradual increase of the network effective conductance under stimulation with a train of pulses (1 ms, 5 V) showing paired-pulse facilitation. Higher pulse frequencies resulted in a more pronounced increase of the network effective conductance.

amplitudes and after 500 μ s from the end of the pulse. Pulses with higher amplitude and longer duration are responsible for stronger potentiation of the effective conductance of the network and slower relaxation dynamics, as evidenced by the less pronounced relaxation after 500 μ s (details in Supplementary Note 5 and Supplementary Figs. 5 and 6).

Notably, the NW network can be successfully stimulated by means of a low-voltage pulse amplitude (<5 V) and down to the microsecond timescale. Moreover, the effective conductance gradually increases when a pulse closely follows a prior pulse emulating paired-pulse facilitation, a process that regulates temporal processing of information in biological neural circuits^{3,40}. As a consequence, multiple pulses applied within short time intervals lead to a frequency-dependent gradual increase of conductivity, with an accumulation effect due to the competition between conductive path formation and spontaneous relaxation (Fig. 2d and Supplementary Fig. 7). Since the influence of distant-past inputs asymptotically fades out over time owing to the short-term memory effect, the NW

network reservoir state depends mostly on recent-past inputs (the echo state property)²⁷.

Nonlinear dynamics, fading memory and temporal processing of multiple spatial inputs with a multi-terminal configuration provide the basis for the implementation as a physical reservoir. RC was demonstrated in a fully memristive architecture based on a NW physical reservoir by solving a pattern recognition task. For this purpose, 4×4 patterns with white (1) or black (0) pixels were converted into a spatio-temporal input by dividing the pattern into four spatial inputs (pattern rows), each containing a four-time-frame input stream (pattern columns), as schematized in Fig. 3a. Each time frame (width of 11 ms) is composed of a 10 ms pulse of 5 V if corresponding to a white pixel, or 0 V (no pulse) if corresponding to a black pixel, followed by 1 ms biased at 0 V. Each input stream was applied to different pads of the multi-terminal NW network reservoir. The reservoir state is represented by the collective state of the three independent output voltages (V_{out}) measured on terminal B of resistances R in series for each input channel under a small d.c. bias

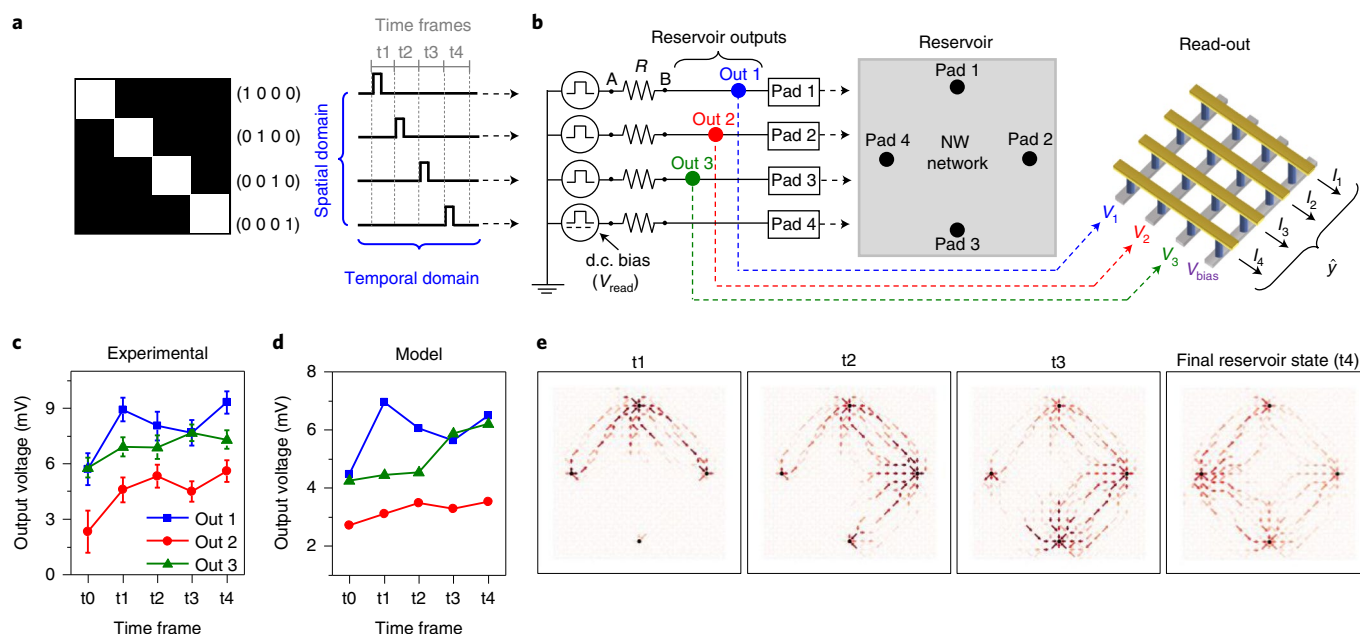


Fig. 3 | Fully memristive RC implementation and spatio-temporal evolution of the NW network reservoir state. **a**, Example of a 4×4 pattern with white (1) and black (0) pixels converted into a spatio-temporal input with four time frames (t_1 – t_4); the spatio-temporal input is fed to the network reservoir in the form of voltage pulses applied to different locations of the network (spatial domain) at different times (temporal domain). **b**, Conceptual schematic representation of the experimental implementation of RC in a fully memristive nanoarchitecture where each temporal pattern is applied to different spatial locations of the network. The input in the form of voltage pulses was applied to terminals A. The reservoir state after stimulation is represented by the collective state of the three independent output voltages V_{out} (Out 1–3 in **b**) on terminals B of series resistances ($R = 82 \Omega$) that were monitored over time by applying a small d.c. read voltage ($V_{read} = 100$ mV) to an arbitrary pad (Pad 4) in addition to the pulse stream. The reservoir output is then passed in form of input voltages (V_1 – V_3) together with a bias (V_{bias}) to a one-layer feed-forward neural network implemented with a cross-point circuit of ReRAM elements (blue cylinders) that are located at the cross-point positions between rows (grey bars) and columns (yellow bars). This ReRAM circuit performs matrix-vector multiplication of the input to obtain the desired output represented by currents I_1 – I_4 . **c,d**, Experimental (**c**) and simulated (**d**) evolution of output voltages after each stimulation time frame of pattern reported in **a**. The time frame 0 represents output voltages of the reservoir state before stimulation (ground state). In **c**, experimental data represent the mean and standard deviation of output voltages obtained by stimulating the NW network 30 times with the same pattern. **e**, Direct visualization by modelling of the evolution of the reservoir state represented by the network conductivity map after each stimulation time frame. Red intensity of edges is proportional to the edge conductance, blue intensity of each node is proportional to the node voltage, arrows indicate the current direction and black nodes represent input pads.

stimulation (100 mV) of a selected channel (Fig. 3b). During classification, the output signals of the final reservoir state (after the termination of the pulse stream) are fed into the 4×4 neural network of ReRAM for read-out (Methods). The read-out output consists of the input voltages multiplied by the conductance weights stored in the cross-point array of ReRAMs obtained by matrix-vector multiplication in the analogue domain with physical multiplication by Ohm's law and physical summation by Kirchhoff's law (Supplementary Figs. 8 and 9)⁴¹. The output neuron with the maximum dot product corresponds to the predicted pattern. Note that the advantage of this configuration is that the same network terminals are used both to stimulate and probe the internal reservoir state, limiting the number of required electrodes if compared a reservoir based on crossbar architecture (Supplementary Fig. 10). Also, the NW-based reservoir allows high scalability, high synapse density and minimization of wiring costs (Supplementary Note 6 and Supplementary Fig. 11). Experimental and modelling studies of the time evolution of the reservoir output voltages are detailed in Supplementary Figs. 12 and 13, Supplementary Table 1 and Supplementary Video 2. Since the multi-terminal NW network reservoir behaviour is regulated by spatio-temporal dynamics with fading memory properties, the reservoir state depends on both the spatial location and temporal sequence of input stimuli (Supplementary Figs. 14 and 15). This results in the temporal information processing capability of multiple spatial inputs of the NW network reservoir.

The experimental evolution of the reservoir outputs during stimulation with the pattern reported in Fig. 3a is reported in Fig. 3c (working principles are detailed in Supplementary Note 7 and Supplementary Fig. 16; experimental and simulated reservoir outputs and conductance maps are detailed in Supplementary Figs. 17 and 18). Figure 3d shows simulation results for the same input signal, indicating a good agreement with the experimental results. Depending on the stimulation pattern, the effect of each stimulation time frame is to induce a peculiar modification of the local conductivity map that depends also on short-term changes induced by the stimulation during previous time frames (accumulation effect), as can be observed by direct visualization of spatio-temporal dynamics of the internal reservoir state (Fig. 3e and Supplementary Video 3).

Thanks to the spatio-temporal information processing capabilities, the NW network was employed for the classification of patterns reported in Fig. 4a. Note that, after each pattern stimulation, the reservoir spontaneously relaxes back to the ground state owing to short-term memory (Supplementary Fig. 19). The corresponding experimental and simulated reservoir outputs after stimulation with each pattern are reported in Fig. 4e–h and Fig. 4i–l, respectively. The reproducibility of the network response is detailed in Supplementary Fig. 20. The results show that the reservoir output voltages and corresponding conductance maps reported in Fig. 4m–p are notably different depending on the specific stimulation pattern,

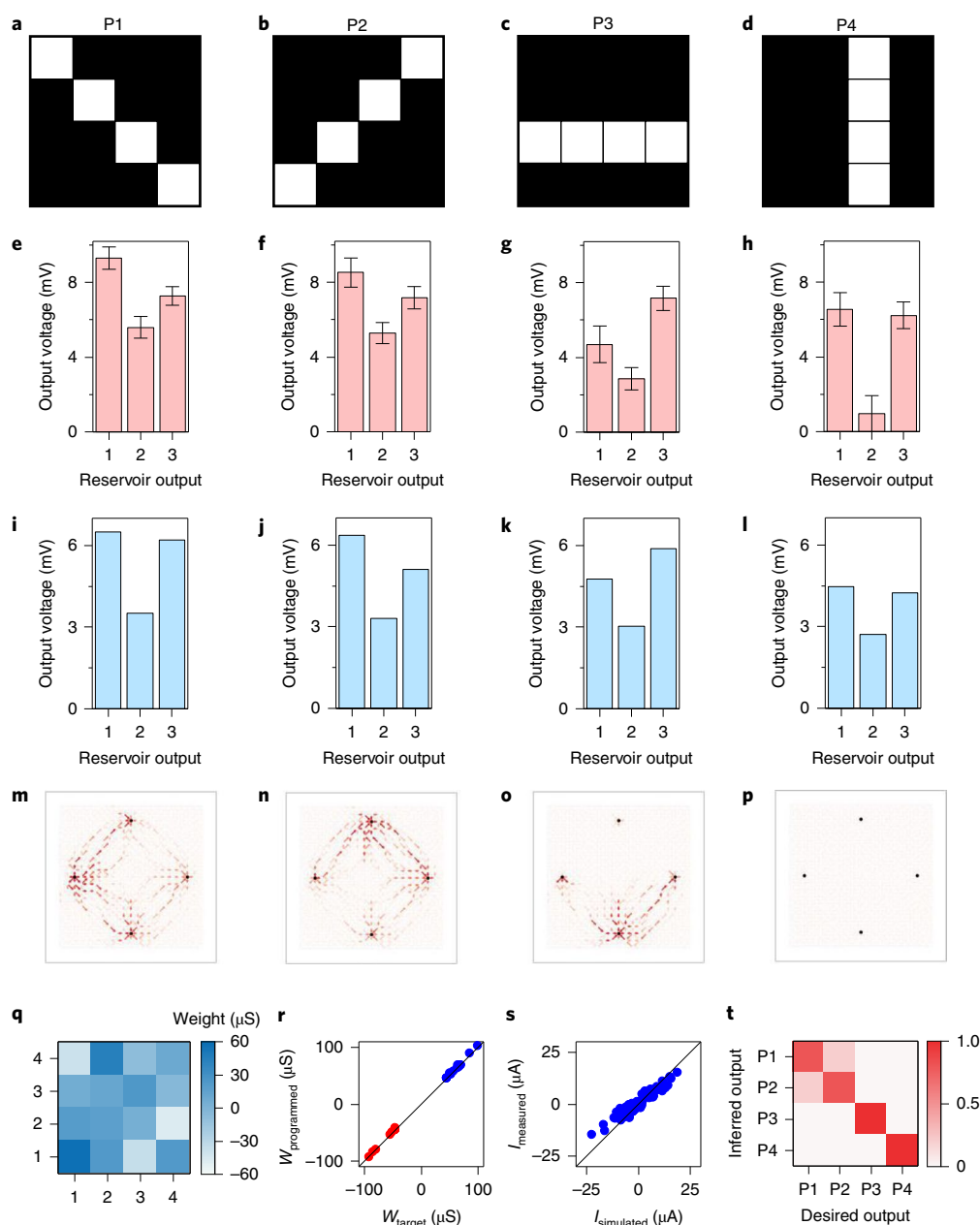


Fig. 4 | Pattern classification with a fully memristive nanoarchitecture based on self-organized memristive NW networks. **a–d**, Patterns (P) considered in this test. **e–h**, Corresponding experimentally measured reservoir outputs after stimulation. **i–l**, Corresponding simulated reservoir outputs after stimulation. Histograms of experimental data represent the mean and standard deviation of output voltages obtained by stimulating the NW network 30 times with each pattern. **m–p**, Conductance maps representing the final reservoir state after stimulation with patterns reported in **a–d**, respectively. Red intensity of edges is proportional to the edge conductance, blue intensity of each node is proportional to the node voltage, arrows indicate the current direction and black nodes represent input pads. **q**, Experimental synaptic weights mapped on a TaO_x ReRAM cross-point circuit after offline training. **r**, Comparison of experimental programmed weights ($W_{\text{programmed}}$) of the read-out with target weights (W_{target} ; negative weights in red, positives in blue), showing that analogue weights are correctly programmed in the TaO_x cross-point circuit. **s**, Comparison between experimentally measured (I_{measured}) and simulated ($I_{\text{simulated}}$) currents of the read-out after weight programming. **t**, Confusion matrix of the fully memristive experimental classification of input patterns. The colour bar represents the occurrence of a given predicted output.

highlighting the reservoir ability to separate these inputs (separability property). Details on the time evolution of reservoir output voltages and conductance maps are reported in Supplementary Figs. 21 and 22, respectively. The experimental reservoir states were used as the input of the memristive read-out function for training and classification, where the accuracy of the fully memristive architecture was evaluated by considering 100 patterns for training and 20 for testing. The experimental synaptic weights mapped on the

TaO_x ReRAM cross-point array after offline training are reported in Fig. 4q. Figure 4r shows the correlation between programmed ReRAM conductance weights and target ones, supporting the accuracy of the read-out network. This is further supported by Fig. 4s, which shows the correlation between the measured read-out current and the simulated one. The experimental inference result is reported in Fig. 4t. The results indicate that the fully memristive architecture correctly classifies the vast majority of input patterns,

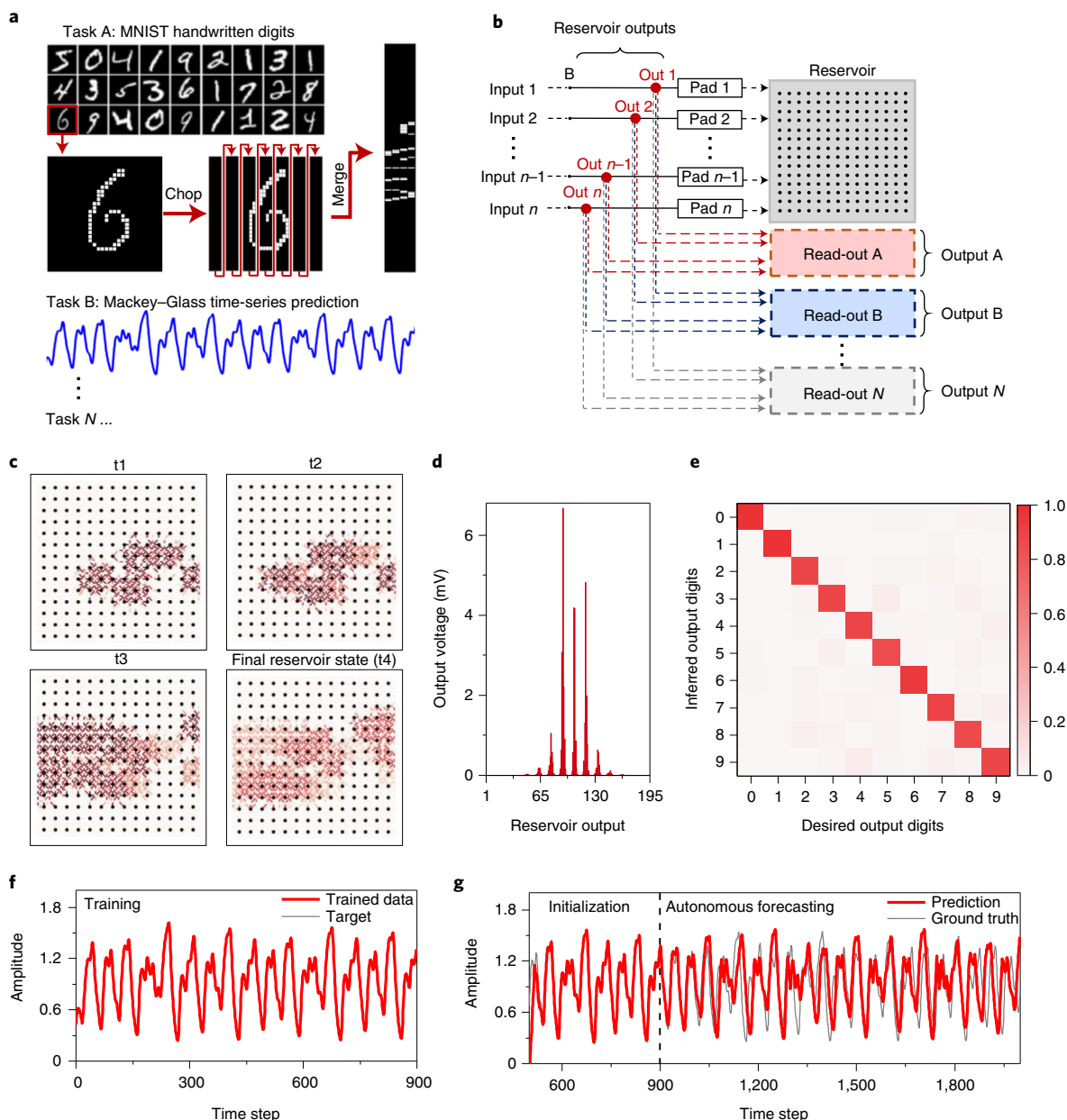


Fig. 5 | NW network reservoir as a generic scalable computational substrate for multiple tasks. **a**, Versatility of the NW network to solve N tasks including MNIST handwritten digit classification (task A; here the original image with 28×28 pixels is binarized, then divided into seven columns and merged in a 196×4 pattern that is converted in 196 pulse streams with four time frames) and Mackey–Glass time-series prediction (task B). **b**, Different tasks can be solved with the same NW network by associating to each task a read-out that can be trained independently, without interfering with what was learned in previous tasks. A NW network with a 14×14 grid of electrodes was considered, where reservoir outputs were collected on terminals B according to the memristive RC implementation of Fig. 3b. **c**, Direct visualization of the evolution of the reservoir state after each time-frame stimulation of digit '6' reported in **a**. **d**, Corresponding reservoir output voltages. In **c**, the red intensity of the edges is proportional to the edge conductance, the blue intensity of each node is proportional to the node voltage, the arrows indicate the current direction and the black nodes represent input pads. **e**, Confusion matrix from inference results on classifying the MNIST test set of 10,000 handwritten digits, after training the read-out with the MNIST training set of 60,000 handwritten digits. The colour bar represents the occurrence of a given predicted output. **f, g**, Training (**f**) and autonomous forecasting (**g**) of the Mackey–Glass time series with the NW network. The ground truth is represented in grey, while the predicted output is in red. The dashed vertical line indicates the transition between initialization and autonomous forecasting.

with an accuracy of 90.0% compared with a software read-out baseline of 95.0% (additional data in Supplementary Fig. 23).

The NW network reservoir represents a generic computational platform for multiple tasks, since a read-out associated to a new task can be learned independently from the read-out that was learned in previous tasks. The scalability and versatility of our *in materia*

RC approach was assessed by simulating an extended NW network for the classification of the complete Modified National Institute of Standards and Technology (MNIST) handwritten digit dataset and for time series prediction (Fig. 5a). Since training occurs only at the read-out, the same NW network reservoir can be exploited for solving multiple tasks, each associated to different parallel

read-outs (Fig. 5b). Also, the same reservoir outputs can be analysed by multiple read-outs, in principle allowing the network to have a multitasking capability.

For the MNIST task, each handwritten digit with 28×28 pixels was first binarized, then chopped into seven columns and merged in a spatio-temporal 196×4 pattern (Supplementary Note 8). Then, the obtained pattern was transformed in 196 pulse streams with four time frames that were applied to 14×14 NW network pads. Finally, reservoir outputs were exploited as read-out input for digit classification (Methods and Supplementary Fig. 24). The spatio-temporal evolution of the reservoir state upon stimulation with a digit '6' as shown in Fig. 5a is reported in Fig. 5c, while final reservoir output voltages after stimulation are reported in the histogram of Fig. 5d (details in Supplementary Video 4; additional data in Supplementary Figs. 25 and 26). After training the read-out with the 60,000 handwritten digits from the MNIST training dataset (Supplementary Fig. 27), the system can correctly classify $\sim 90.4\%$ of the 10,000 MNIST digits from the test set. Note that the memristive NW network reservoir outperforms the static network (Supplementary Note 9 and Supplementary Fig. 28), although its accuracy decreases if the final reservoir state loses information from the initial stimulation time frames (Supplementary Fig. 29). The confusion matrix is reported in Fig. 5e and detailed in Supplementary Table 2. Misclassifications were mainly related to digits that are hardly distinguishable due to low pixel resolution and to the partial loss of information during the binarization of greyscale images (Supplementary Fig. 30). Since the spatial information is encoded in the spatio-temporal domain and the physical reservoir does not require training, the main advantage of this nanoarchitecture is the reduction of network size and training cost (Supplementary Note 10). Note that the accuracy is notably higher than in previously presented one-shot memristor-based RC systems³⁶, while accuracy can be further increased with multiple reads during the reservoir computation³⁴, at the cost of a quadratic increase in computational complexity (Supplementary Note 11).

The RC architecture is also suitable for the prediction of purely time-dependent tasks such as a Mackey–Glass time series, a chaotic system that has a deterministic form but is considered difficult to predict with conventional machine-learning algorithms^{12,43}. The Mackey–Glass task has been implemented by presenting an initial teacher signal generated by the Mackey–Glass equation, followed by the prediction by the trained system of the time series some steps ahead. Figure 5f,g reports the results of autonomous time-series prediction, which was performed by considering multiple reservoir output nodes and the virtual node method for delayed feedback systems^{17,34,44} (details in Methods and Supplementary Fig. 31). In Fig. 5f, it can be observed that the target and the predicted value during the training process match accurately (accuracy $\approx 100\%$), showing that the trained read-out weights are able to calculate the next time-step signal based on the reservoir outputs. After initialization, the network was used to predict the time series autonomously (Fig. 5g). After time step 900, the read-out output (the predicted signal) is fed as the new input to the reservoir state in a closed feedback loop. As a result, the system can autonomously and continuously produce the time series that was observed to match well with the expected ground truth, which is shown in the plot as a reference (trace plots in the phase space in Supplementary Fig. 32). After a few hundred time steps of accurate time series prediction (accuracy of $\sim 90.6\%$ over 100 time steps), deviations from the ground truth start to occur due to the accumulation of small errors in the autonomous prediction, with a consequent phase shift. Despite the loss of accuracy, the predicted signal still maintains the main features and temporal dynamics of the Mackey–Glass time series. Long-term prediction can be achieved by periodically updating the NW network reservoir, avoiding divergence of the system to the chaotic ground truth (Supplementary Fig. 33).

Depending on the specific task, the accuracy of the system can be further improved by optimizing the stimulating parameters that regulate the NW network nonlinear response, such as pulse amplitude, width and rates. Also, the physical reservoir can be further simplified by compensating for the reduction of physical nodes (number of electrodes) by introducing virtual nodes⁴⁴. Note also that the RC capabilities are not hindered by non-idealities including local variations of the NW density that lead to a non-homogeneous conductivity map over the NW network⁴⁵ and/or by the junction-to-junction variability of the memristive behaviour¹². Indeed, these effects that lead to a different nonlinear response of different areas of the network can enhance the extraction of relevant features from the reservoir. Such non-idealities can even be beneficial for the computing performances^{34,46}. This opens the possibility of locally controlling the topology and memristive response of the network to optimize computing performances on specific tasks. Also, the number of reservoir inputs/outputs is limited only by the number of contacts that can be realized, which supports the possibility of designing cost-effective neuromorphic nanoarchitectures able to process a large number of spatio-temporal inputs. Although the power consumption of our NW-based physical reservoir is higher than state-of-the-art top-down memristive RC systems, the energy efficiency can be largely optimized by properly engineering the NW core-shell structure to reduce the switching/operating currents (Supplementary Note 12). However, this network-type reservoir based on NW networks is able to process multiple inputs by experiencing synaptic plasticity at many spatial and temporal scales from microseconds up to hundreds of seconds depending on the input stimuli, as required to reach the potential of brain-derived computing⁴⁷. For this reason, this low-cost physical reservoir can be explored for a wide range of applications, including speech recognition, natural language analysis, motion identification and processing of multiple sensorial inputs for robotics. For all these challenging computing tasks, a versatile implementation design of a large-scale NW-based fully memristive system is proposed in Supplementary Fig. 34.

In conclusion, a fully memristive RC architecture was implemented in hardware by using a memristive NW network acting as a network-wide reservoir. Similar to biological organisms, computational properties of the network emerge as a collective property of the self-organizing and highly connected system, having a large number of interacting components (memristive elements). The recognition of spatio-temporal patterns was demonstrated by coupling the NW network with a memristive read-out network of ReRAM devices, where data processing in both the reservoir and read-out was performed in the hardware. In particular, the computing capabilities of the NW network physical reservoir were demonstrated by classification of the MNIST handwritten digit dataset and Mackey–Glass time-series prediction. These results pave the way for the *in materia* implementation of brain-inspired unconventional computing paradigms, thanks to the exploitation of emergent memristive behaviour in self-organizing NW networks combined with top-down ReRAM devices, towards the realization of general-purpose intelligent systems that combine different neuromorphic hardware technologies with the aim of artificial general intelligence.

Online content

Any methods, additional references, Nature Research reporting summaries, source data, extended data, supplementary information, acknowledgements, peer review information; details of author contributions and competing interests; and statements of data and code availability are available at <https://doi.org/10.1038/s41563-021-01099-9>.

Received: 3 February 2021; Accepted: 9 August 2021;
Published online: 4 October 2021

References

1. Mead, C. Neuromorphic electronic systems. *Proc. IEEE* **78**, 1629–1636 (1990).
2. Wang, Z. et al. Resistive switching materials for information processing. *Nat. Rev. Mater.* **5**, 173–195 (2020).
3. Milano, G. et al. Self-limited single nanowire systems combining all-in-one memristive and neuromorphic functionalities. *Nat. Commun.* **9**, 5151 (2018).
4. Wang, Z. et al. Memristors with diffusive dynamics as synaptic emulators for neuromorphic computing. *Nat. Mater.* **16**, 101–108 (2017).
5. Jo, S. H. et al. Nanoscale memristor device as synapse in neuromorphic systems. *Nano Lett.* **10**, 1297–1301 (2010).
6. Xia, Q. & Yang, J. J. Memristive crossbar arrays for brain-inspired computing. *Nat. Mater.* **18**, 309–323 (2019).
7. Lin, P. et al. Three-dimensional memristor circuits as complex neural networks. *Nat. Electron.* **3**, 225–232 (2020).
8. Kandel, E. R., Schwartz, J. H., Jessell, T. M., Siegelbaum, S. A. & Hudspeth, A. J. *Principles of Neural Science* 5th edn (McGraw-Hill Professional, 2013).
9. Essen, V. & Tognoli, G. in *Fundamentals of Brain Network Analysis* (eds Fornito, A. et al.) 1–35 (Elsevier, 2016); <https://doi.org/10.1016/B978-0-12-407908-3.00001-7>
10. Suárez, L. E., Markello, R. D., Betzel, R. F. & Misic, B. Linking structure and function in macroscale brain networks. *Trends Cogn. Sci.* **24**, 302–315 (2020).
11. Stieg, A. Z. et al. Emergent criticality in complex Turing B-type atomic switch networks. *Adv. Mater.* **24**, 286–293 (2012).
12. Milano, G. et al. Brain-inspired structural plasticity through reweighting and rewiring in multi-terminal self-organizing memristive nanowire networks. *Adv. Intell. Syst.* <https://doi.org/10.1002/aisy.202000096> (2020).
13. Tanaka, H. et al. A molecular neuromorphic network device consisting of single-walled carbon nanotubes complexed with polyoxometalate. *Nat. Commun.* **9**, 2693 (2018).
14. Pike, M. D. et al. Atomic scale dynamics drive brain-like avalanches in percolating nanostructured networks. *Nano Lett.* **20**, 3935–3942 (2020).
15. Diaz-Alvarez, A. et al. Emergent dynamics of neuromorphic nanowire networks. *Sci. Rep.* **9**, 14920 (2019).
16. Sillin, H. O. et al. A theoretical and experimental study of neuromorphic atomic switch networks for reservoir computing. *Nanotechnology* **24**, 384004 (2013).
17. Fu, K. et al. in *2020 International Joint Conference on Neural Networks (IJCNN)* 1–8 (IEEE, 2020); <https://doi.org/10.1109/IJCNN48605.2020.9207727>
18. Milano, G., Porro, S., Valov, I. & Ricciardi, C. Recent developments and perspectives for memristive devices based on metal oxide nanowires. *Adv. Electron. Mater.* **5**, 1800909 (2019).
19. Bose, S. K. et al. Evolution of a designless nanoparticle network into reconfigurable Boolean logic. *Nat. Nanotechnol.* **10**, 1048–1052 (2015).
20. Demis, E. C. et al. Nanoarchitectonic atomic switch networks for unconventional computing. *Jpn J. Appl. Phys.* **55**, 1102B2 (2016).
21. Massey, M. K. et al. Evolution of electronic circuits using carbon nanotube composites. *Sci. Rep.* **6**, 32197 (2016).
22. Hochstetter, J. et al. Avalanches and edge-of-chaos learning in neuromorphic nanowire networks. *Nat. Commun.* **12**, 4008 (2021).
23. Zhu, R. et al. Information dynamics in neuromorphic nanowire networks. *Sci. Rep.* **11**, 13047 (2021).
24. Lilak, S. et al. Spoken digit classification by in-materio reservoir computing with neuromorphic atomic switch networks. *Front. Nanotechnol.* <https://doi.org/10.3389/fnano.2021.675792> (2021).
25. Jaeger, H. *The 'Echo State' Approach to Analysing and Training Recurrent Neural Networks* GMD Technical Report 148 (German National Research Center for Information Technology, 2001).
26. Maass, W., Natschläger, T. & Markram, H. Real-time computing without stable states: a new framework for neural computation based on perturbations. *Neural Comput.* **14**, 2531–2560 (2002).
27. Tanaka, G. et al. Recent advances in physical reservoir computing: a review. *Neural Netw.* **115**, 100–123 (2019).
28. Nakajima, K. Physical reservoir computing—an introductory perspective. *Jpn J. Appl. Phys.* **59**, 060501 (2020).
29. Torrejon, J. et al. Neuromorphic computing with nanoscale spintronic oscillators. *Nature* **547**, 428–431 (2017).
30. Prychynenko, D. et al. Magnetic skyrmion as a nonlinear resistive element: a potential building block for reservoir computing. *Phys. Rev. Appl.* **9**, 014034 (2018).
31. Vandoorne, K. et al. Experimental demonstration of reservoir computing on a silicon photonics chip. *Nat. Commun.* **5**, 3541 (2014).
32. Van der Sande, G., Brunner, D. & Soriano, M. C. Advances in photonic reservoir computing. *Nanophotonics* **6**, 561–576 (2017).
33. Du, C. et al. Reservoir computing using dynamic memristors for temporal information processing. *Nat. Commun.* **8**, 2204 (2017).
34. Moon, J. et al. Temporal data classification and forecasting using a memristor-based reservoir computing system. *Nat. Electron.* **2**, 480–487 (2019).
35. Zhu, X., Wang, Q. & Lu, W. D. Memristor networks for real-time neural activity analysis. *Nat. Commun.* **11**, 2439 (2020).
36. Midya, R. et al. Reservoir computing using diffusive memristors. *Adv. Intell. Syst.* **1**, 1900084 (2019).
37. Zhong, Y. et al. Dynamic memristor-based reservoir computing for high-efficiency temporal signal processing. *Nat. Commun.* **12**, 408 (2021).
38. Manning, H. G. et al. Emergence of winner-takes-all connectivity paths in random nanowire networks. *Nat. Commun.* **9**, 3219 (2018).
39. Li, Q. et al. Dynamic electrical pathway tuning in neuromorphic nanowire networks. *Adv. Funct. Mater.* **30**, 2003679 (2020).
40. Jackman, S. L. & Regehr, W. G. The mechanisms and functions of synaptic facilitation. *Neuron* **94**, 447–464 (2017).
41. Ielmini, D. & Wong, H.-S. P. In-memory computing with resistive switching devices. *Nat. Electron.* **1**, 333–343 (2018).
42. Mackey, M. & Glass, L. Oscillation and chaos in physiological control systems. *Science* **197**, 287–289 (1977).
43. Jaeger, H. Harnessing nonlinearity: predicting chaotic systems and saving energy in wireless communication. *Science* **304**, 78–80 (2004).
44. Appeltant, L. et al. Information processing using a single dynamical node as complex system. *Nat. Commun.* **2**, 468 (2011).
45. Milano, G. et al. Mapping time-dependent conductivity of metallic nanowire networks by electrical resistance tomography toward transparent conductive materials. *ACS Appl. Nano Mater.* <https://doi.org/10.1021/acsanm.0c02204> (2020).
46. Burger, J. & Teuscher, C. in *2013 IEEE/ACM International Symposium on Nanoscale Architectures (NANOARCH)* 1–6 (IEEE, 2013); <https://doi.org/10.1109/NanoArch.2013.6623028>
47. Aimone, J. B. A roadmap for reaching the potential of brain-derived computing. *Adv. Intell. Syst.* <https://doi.org/10.1002/aisy.202000191> (2020).

Publisher's note Springer Nature remains neutral with regard to jurisdictional claims in published maps and institutional affiliations.

© The Author(s), under exclusive licence to Springer Nature Limited 2021

Methods

Fabrication of memristive NW networks. NW networks were realized by drop-casting Ag NWs with a diameter of 115 nm and length of 20–50 μm in isopropyl suspension (from Sigma-Aldrich) on a SiO_2 (1 μm)/Si commercial substrate (Supplementary Fig. 1). The structural topology of the network was characterized by means of field-emission SEM (Zeiss Merlin FESEM). Structural and chemical characterization of Ag NWs, performed in our previous work¹² by means of transmission electron microscopy and X-ray photoelectron spectroscopy, revealed that these NWs are characterized by the presence of a PVP shell layer of ~1–2 nm surrounding the Ag NW core. The presence of this shell layer is a direct consequence of the polyol synthesis process, where this polymer is used as a surfactant to control the morphology of these nanostructures. Besides acting as a memristive shell, the PVP layer contributes also to the chemical stability of the Ag NW inner core, preventing its direct contact with the surrounding atmosphere. Memristive NW networks with an areal mass density of 41 mg m^{-2} were realized by controlling the concentration of Ag NWs in the suspension and by fixing the drop volume deposited on a 12 \times 12 mm^2 area to 20 μl in order to ensure homogeneous distribution of NWs all over the sample⁴⁵. Electrical contacts on the NW network were realized by deposition of Au pads by sputtering and shadow masking (thickness of 250 nm, approximate size of 1.2 \times 0.3 mm).

Memristive read-out fabrication. The ReRAM cross-point array for hardware implementation of the memristive read-out is fabricated by electron-beam evaporation of a TaO_x active layer (3 nm, root mean squared roughness <0.3 nm) sandwiched between a Pt bottom electrode and a Ta/Ti top electrode, again realized by electron-beam evaporation. The oxide layer and the top electrode are evaporated without breaking the vacuum. The ReRAM array was composed of different columns of single cross-point cells that were wire-bonded to recreate a fully connected cross-point array (Supplementary Fig. 2).

Electrical characterization of NW network. Electrical measurements in the two-terminal configuration reported in Fig. 2 were performed by contacting Au pads separated by ~7 mm with electrical probes in a SemiProbe probe station coupled with a Keithley 4200 semiconductor device analyser equipped with pulse measuring units. The conductance weight change reported in Fig. 2c was evaluated as $\Delta w = (G_2 - G_1)/G_1$, where G_2 is the effective conductance evaluated at the end of stimulation or 500 μs after stimulation, while G_1 is the effective conductance before stimulation as schematized in Supplementary Fig. 6. To monitor the spontaneous relaxation process of the network after stimulation, stress voltages in the range of 10–50 mV were applied to minimize the influence of the bias voltage on the relaxation process, ensuring at the same time the recording of a high signal-to-noise current time trace. All measurements were performed in air at room temperature.

NW network modelling. Modelling of the spatio-temporal evolution of the memristive NW network was performed in Python exploiting the NetworkX package. For this purpose, the NW network was modelled as a regular grid graph with random diagonals where the edge dynamics with a short-term memory effect are described with a physics-based potentiation–depression rate balance equation⁴⁸. Pads were placed on the grid graph according to the geometry of the considered experimental NW network sample. Details of the NW network representation with a grid-graph model are reported in Supplementary Fig. 4 and Supplementary Note 3, while the state equation regulating the edge dynamics is described in Supplementary Note 4. Parameters of the model extrapolated from experimental data are reported in Supplementary Table 1.

Experimental set-up for multi-terminal measurements and RC. The NW network device was bonded on a custom package and connected to a printed circuit board. A TTI TGA1242 four-channel arbitrary waveform generator acting as a voltage buffer was used to generate the input signal and connected to the four A terminals of input resistance $R = 82 \Omega$, whose B terminal was directly connected to the NW network pads (Fig. 3b). The arbitrary waveform generator was programmed such that the output impedance was fixed at 50 Ω and comparable to R . A Tektronix MSO58 eight-channel oscilloscope was used to monitor the circuit voltages by means of high-impedance probes connected to the B terminals of the input resistances. For each resistance, two probes were connected to monitor the voltage developed across the NW network during both the set operation, which usually shows relatively large currents, and the read operation, which typically drains a lower current. The read of the reservoir output voltages for each time frame during pattern classification was performed according to Supplementary Fig. 16, where the final reservoir state after stimulation to be passed to the read-out for classification corresponds to the reservoir output voltages at time frame t4. Note that, for n input channels, only $n - 1$ output voltages are independent, according to Kirchhoff's law.

Read-out training. The memristive read-out function for spatio-temporal pattern recognition was offline trained through supervised learning by minimizing the categorical cross-entropy loss function (L):

$$L = - \sum_{i=1}^N y_i \log(\hat{y}_i) \quad (1)$$

where N is the dimension of the output size, y_i is the desired target and \hat{y}_i is the read-out model prediction. The minimization of the loss function performed in a Python environment has been achieved according to the Adam algorithm⁴⁹, which relies on the optimization of a stochastic gradient-descent method by the adaptive tuning of the learning rates for the different parameters to train. Parameters are updated at each step t according to

$$w_{t+1} = w_t - \frac{\eta}{\sqrt{\hat{v}_t} + \epsilon} \hat{m}_t \quad (2)$$

where \hat{m}_t and \hat{v}_t are the bias-corrected estimates of first and second moment of the gradients, respectively, while η and ϵ are parameters. For each epoch, equation (2) is iterated over all the training dataset subsets. Typically, the epoch number to obtain a good convergence of the model has been set to 2,000. The read-out was trained with linear regression for Mackey–Glass time-series prediction.

Memristive read-out classification. The reservoir state has been classified by means of a simple one-layer neural network read-out function implemented in hardware in a ReRAM array. The one-layer neural network read-out is fully connected, and neurons are activated through the softmax (\hat{S}) nonlinear function. The model predicts the results to be

$$\hat{y} = \hat{S}(Ax + b) \quad (3)$$

where A is the neural network weights matrix and b is the bias vector that was implemented in hardware in the TaO_x ReRAM cross-point array, while x is the read-out input. As read-out inputs, the standardized reservoir outputs (by removing the mean value and scaling to the unit variance) were passed as voltage inputs to the read-out function. In the read-out memristive circuit, the synaptic weight W is mapped by a pair of conductance values, G^+ and G^- , biased at positive and negative voltages, respectively, and the synaptic weight is described by the equivalent conductance, $G^+ - G^-$ (ref. 50). Synaptic weights were linearly mapped in the range 45–100 μS to ensure device stability, while the input read-out voltage amplitude was linearly mapped in the range 0.01–0.31 V. The ReRAM devices in each column were first formed, then they were connected to the external pads of a package by wire bonding and finally they were operated in a cross-point fashion; for example, the top electrodes of the first cell in each column were all short-circuited to form the first row of the ReRAM array. The cross-point operation was executed by a switch matrix enabling the reconfigurable connection of all terminals. The weights G_{ij} were then programmed in the cross-point array in differential mode, where a synaptic weight was obtained by programming a positive conductance G^+ in a cell and a negative conductance G^- in another cell, to obtain the desired weight $G_{ij} = G^+ - G^-$. Finally, the voltage signal was applied at the row terminals, and the column currents were collected to enable physical summation according to Kirchhoff's law. An Agilent B1500 semiconductor parameter analyser was used for programming the ReRAM devices in the desired weights via a quasi-static programming pulse. A program and verify algorithm was used to correctly program the analogue weights, by targeting a conductance G_{target} and applying set/reset pulses until convergence upon a given tolerance $\pm 5\%$. A Keithley 707 switch matrix was used to allow access to any device in a random fashion and connect the cross-point array with common rows/columns in a crossbar. A TTI TGA1252 four-channel arbitrary waveform generator was used to generate analogue vectors corresponding to the output of the reservoir layer, to apply to the cross-point array columns, while the rows were kept at ground through a low impedance input of a Tektronix MSO58 eight-channel oscilloscope, which was used also for monitoring the currents.

Classification of handwritten digits of the MNIST dataset. Classification of the MNIST handwritten digit dataset was performed by modelling the NW network as a grid graph with 29 \times 29 nodes, where the properties of memristive edges were extrapolated from experimental measurements (Supplementary Fig. 4). The stimulation was performed by arranging the $n = 196$ input electrodes in a 14 \times 14 array, as schematized in Fig. 5b. The input pads are numbered from left to right, from top to bottom. The reservoir state after stimulation is represented by the output voltage drop (V_{out}) on a series resistance ($R = 82 \Omega$) that was monitored over time by applying a small d.c. voltage bias ($V_{\text{read}} = 100 \text{ mV}$) to an arbitrary selected electrode (positioned at eighth column from left, seventh row from bottom of the electrode grid in Fig. 5b), reproducing the experimental set-up reported in Fig. 3b with 195 ($n - 1$) independent output voltages. Training and inference were performed according to the experimental procedure described before with a software read-out function. Details on training are reported in Supplementary Fig. 27.

Mackey–Glass time-series prediction. Time-series prediction was demonstrated by considering the Mackey–Glass time series described by the time-delayed differential equation:

$$\frac{dx}{dt} = \beta \frac{x(t - \tau)}{1 + (x(t - \tau))^n} - \gamma x(t).$$

This equation can display a wide range of chaotic behaviours, depending on the values of the parameters. The Mackey–Glass time series was normalized and

transformed to an input voltage signal (in the range 1–6 V) to be presented to the NW network reservoir system by using a chessboard scheme, as schematized in Supplementary Fig. 31. To increase the accuracy prediction of the system, the reservoir dynamics were expanded (1) by considering the response of multiple reservoir output nodes that result in qualitatively similar but quantitatively different responses to the same input (Supplementary Fig. 31), and (2) by using the virtual node method for delayed feedback systems⁴⁸. Autonomous time-series prediction using the NW network-based system was obtained by considering the output of 98 reservoir outputs and 20 virtual nodes, by setting the parameters $\beta=0.2$, $\gamma=0.9$, $n=10$ and $\tau=18$ that correspond to chaotic dynamics (chaotic behaviours can be observed for $\tau>16.8$). Before autonomous prediction, since the chaotic time series strongly depends on the initial conditions, the network (initially in the pristine state) was excited during an initialization step by sending the true input without training. The performance accuracy of the Mackey–Glass time-series prediction was evaluated as $1 - \text{RMSE}$, where RMSE represents the root mean square error.

Data availability

The data that support the findings of this study are available on Zenodo (<https://doi.org/10.5281/zenodo.5153335>). All other data are available from the authors.

Code availability

The codes used to generate datasets of simulations can be accessed on GitHub (https://github.com/MilanoGianluca/Nanowire_Network_Reservoir_Computing).

References

48. Miranda, E., Milano, G. & Ricciardi, C. Modeling of short-term synaptic plasticity effects in ZnO nanowire-based memristors using a potentiation-depression rate balance equation. *IEEE Trans. Nanotechnol.* **19**, 609–612 (2020).
49. Kingma, D. P. & Ba, J. Adam: a method for stochastic optimization. *3rd International Conference for Learning Representations* <https://arxiv.org/abs/1412.6980> (2014).
50. Ielmini, D. & Pedretti, G. Device and circuit architectures for in-memory computing. *Adv. Intell. Syst.* (2020).

Acknowledgements

We acknowledge support by M. Raimondo in helping with SEM measurements. Device fabrication was performed at Nanofacility Piemonte, a facility supported by the

Compagnia di San Paolo foundation, and at PoliFAB, the micro- and nanofabrication facility of Politecnico di Milano. Part of this work was supported by the European project MEMQuD, code 20FUN06. This project (EMPIR 20FUN06 MEMQuD) has received funding from the European Metrology Programme for Innovation and Research (EMPIR) cofinanced by the participating states and from the European Union's Horizon 2020 research and innovation programme. This article received funding from the European Union's Horizon 2020 research and innovation program (grant agreement no. 824164).

Author contributions

G.M., D.I. and C.R. generated the idea and designed the experiments. G.M. performed NW network fabrication and characterization. G.P. and G.M. performed multielectrode NW network characterization. S.R. and S.H. performed fabrication and characterization of the ReRAM read-out. G.M. and K.M. developed the NW network model and performed RC simulations. G.M., K.M. and G.P. analysed data. G.M. and C.R. prepared the manuscript. L.B., D.I. and C.R. supervised the research. All authors participated in the discussion of results and revision of the manuscript.

Competing interests

The device configuration and implementation method of reservoir computing are currently under patent filing (Italian priority application number 102021000019277). Patent applicants: Politecnico di Torino, Politecnico di Milano, Istituto Nazionale di Ricerca Metrologica; Inventors: G.M., G.P., K.M., D.I. and C.R.

Additional information

Supplementary information The online version contains supplementary material available at <https://doi.org/10.1038/s41563-021-01099-9>.

Correspondence and requests for materials should be addressed to Gianluca Milano, Daniele Ielmini or Carlo Ricciardi.

Peer review information *Nature Materials* thanks John Boland and the other, anonymous, reviewer(s) for their contribution to the peer review of this work.

Reprints and permissions information is available at www.nature.com/reprints.